Journal of the Mechanics and Physics of Solids 143 (2020) 104065

Contents lists available at ScienceDirect

Journal of the Mechanics and Physics of Solids

journal homepage: www.elsevier.com/locate/jmps

Non-reciprocal Rayleigh waves in elastic gyroscopic medium

Yuchen Zhao [a], Xiaoming Zhou [a,*], Guoliang Huang [b]

[a] Key Laboratory of Dynamics and Control of Flight Vehicle, Ministry of Education and School of Aerospace Engineering, Beijing Institute of Technology, Beijing 100081, China

[b] Department of Mechanical and Aerospace Engineering, University of Missouri, Columbia, MO 65211, United States

ARTICLE INFO

Article history:
Received 27 January 2020
Revised 21 May 2020
Accepted 20 June 2020
Available online 23 June 2020

Keywords:
Gyroscopic medium
Non-reciprocal Rayleigh waves
One-way edge state
Quantum Hall effect
Stroh formalism

ABSTRACT

The homogenized medium of the gyro lattice with the mechanical quantum Hall effect, here denoted as the gyroscopic elastic medium, is governed by a new set of elastodynamic equations with the chiral density. This paper presents a generic theory based on the Stroh formalism to disclose the non-reciprocal Rayleigh waves supported by the gyroscopic medium. The Stroh formulation is investigated in the general case of anisotropic elasticity, and after introducing the chiral density, it is extended to yield new forms of eigenvalue equations, which are distinct for surface waves traveling in opposite directions. Numerical examples are performed in the isotropic elasticity scheme, illustrating the non-reciprocal Rayleigh waves as well as the evolution of the particle motion trajectory and polarization at shallow depths as the gyro coupling magnitude increases. The developed theory confirms the prediction for the classical Rayleigh wave that is reciprocal when the gyro coupling term vanishes. Finally, a general effective-medium method that relies on the surface response to external excitation is proposed for the estimation of the overall properties of gyroscopic composite materials in the long-wavelength regime. Consistency in the wave response of gyroscopic composites with periodic inclusions and their effectively homogeneous materials is demonstrated for a large range of gyro coupling constants.

1. Introduction

Rayleigh waves, named after its predictive discovery in 1885 by Lord Rayleigh, refer to a type of surface acoustic waves that could propagate near the free surface of solids with rapid amplitude decay in depth (Rayleigh, 1885). Rayleigh waves have proven to be of primary concern in many circumstances. They are important parts of ultrasonic devices, used for materials characterization and defects/cracks detection, or signal processing to change an input electric signal into the required spectrum. In seismology, the understanding of Rayleigh waves caused by earthquakes has been of great importance in preventing severe damage to infrastructures. Highly used in these applications, the control of this type of surface wave has been of longstanding interest in both scientific and engineering communities. In the past century, advances in artificial materials and manufacturing have provided a broad degree of freedom in tailoring the behavior of these surface waves, making it

* Corresponding author.
E-mail address: zhxming@bit.edu.cn (X. Zhou).

https://doi.org/10.1016/j.jmps.2020.104065
0022-5096/

possible to manipulate vibration magnitude, wave speed, polarization mode, and frequency response in terms of designing specific microstructures of a hosting medium or decorating the complex geometry (such as pillars, holes, grooves, and resonators) on the object's surface (Assouar and Oudich, 2011; Colquitt et al., 2017; Li et al., 2018; Wu et al., 2004; Zhou et al., 2014).

Despite decades of research on the manipulation of Rayleigh waves, few strategies have been developed for the breaking of the reciprocal theorem so that different wave velocities can be observed in two opposite directions, or more particularly the waves are only allowed to propagate in specific directions. In principle, this non-reciprocal behavior may provide a wider degree of freedom to manipulate Rayleigh waves for more advanced applications, such as in non-destructive detection, signal processing, and seismic wave mitigation. The wave reciprocity is warranted by the time-reversal symmetry of the material/structure systems. In electronic media, the quantum Hall effect (QHE) arises when the time-reversal symmetry is broken, resulting in the one-way edge modes of currents in two-dimensional (2D) electron systems subject to a perpendicular magnetic field (Haldane, 1988; Hasan and Kane, 2010). Owing to the analogies between electromagnetic and mechanical scattering processes, specially designed mechanical structures to break the time-reversal symmetry have been recently reported (Chen et al., 2019; Ding et al., 2019; Fleury et al., 2014; Nash et al., 2015; Wang et al., 2015). One of the mechanical QHE analogs consisted of a periodic lattice loaded with a spinning gyroscope (Brun et al., 2012; Milton and Willis, 2007). The angular momentum effect of gyros led to the chiral coupling of the inertial motion, which played an analogous role to the biasing magnetic field in the quantum Hall system. As a result, the gyro periodic lattice possessed the same topologically protected one-way edge state that was robust against the surface defects (Nash et al., 2015; Wang et al., 2015).

In the long-wavelength limit, the gyro lattice with a mechanical QHE can be equivalently represented by the Cauchy elastic medium with the Hermite density (Brun et al., 2012; Carta et al., 2014). This new set of equation systems may have helped to provide an understanding of unidirectional surface waves through setting up analytical surface state equations, similar to the formulation of Rayleigh wave equations in the pioneering work by Lord Rayleigh (Rayleigh, 1885). As a preliminary exploration of this issue, we have verified theoretically the existence of unidirectional surface states of the imaginary "gyroscopic fluids" that possess the Hermite density, yet don't support the shearing (Zhou and Zhao, 2019). Acoustic wave in fluids is only relevant to the longitudinal mode. However, solids that withstand shear involve both the longitudinal and transverse modes, and in particular, for gyroscopic elastic solids, these two wave modes are strongly coupled due to the chiral inertial effect. This inherently different wave coupled phenomenon makes the characterization of non-reciprocal Rayleigh waves much more complicated and cannot be simply captured from the method in the prior work (Zhou and Zhao, 2019). To address this challenge, the Stroh formalism (Stroh, 1962) is adopted and extended, which has proven to be an efficient method for analyzing the structure and existence of surface waves in classical elastic media. Compared to the previously developed formalism of the Stroh method (Chadwick and Smith, 1977; Fu, 2007; Fu et al., 2013; Parker, 2013; Tanuma, 2007), the modified Stroh formalism in the present work can efficiently take into account the chiral inertial coupling in gyroscopic solids. Here, the fundamental solution of the non-reciprocal Rayleigh wave with the Stroh's eigen-matrix is formulated in a complex domain for the first time.

The paper is organized as follows. In Section 2, the Stroh formalism is extended to solve the surface state of the gyroscopic continuum in the most general case of anisotropic elasticity. Equations and conditions for the existence of surface states will be derived. In Section 3, the isotropic elasticity case of the generic theory in Section 2 is described and numerical examples are conceived to demonstrate non-reciprocal Rayleigh waves supported by gyroscopic elastic continua. In Section 4, the non-reciprocal Rayleigh wave phenomena are studied in a periodic structure consisting of gyroscopic inclusions embedded in an elastic matrix. A general homogenization method for retrieving effective elastic parameters and chiral densities is presented. The conclusions are outlined in Section 5.

2. Stroh formalism for elastodynamic systems with chiral density

2.1. Description of the problem

Consider a 2D elastic gyroscopic medium in plane strain that occupies a semi-infinite space as shown in Fig. 1. The equation of inertial motion of elastic gyroscopic medium follows from (Brun et al., 2012; Carta et al., 2014)

$$\nabla \cdot \boldsymbol{\sigma} = \boldsymbol{\rho} \partial^2 \mathbf{u} / \partial t^2, \tag{1}$$

where $\boldsymbol{\sigma}$ is the Cauchy stress tensor and $\mathbf{u}$ is the displacement vector. The density tensor $\boldsymbol{\rho}$ takes the chiral form

$$[\boldsymbol{\rho}] = \begin{bmatrix} \rho & i\alpha \\ -i\alpha & \rho \end{bmatrix}, \tag{2}$$

where ρ is the inertial density, and the off-diagonal elements describe the coupling between longitudinal and lateral motions with the imaginary unit denoting the phase shift between the gyroscopic force and displacement. The spinner constant α is related to the characteristic length and moment of inertia of the gyroscope (Brun et al., 2012), and α could be real positive or negative value to describe the inversion of the spinning direction of the gyroscope. The constitutive equation of the gyroscopic medium in the most general case of anisotropic elasticity is given by

$$\boldsymbol{\sigma} = \mathbf{C} : \boldsymbol{\varepsilon}, \tag{3}$$

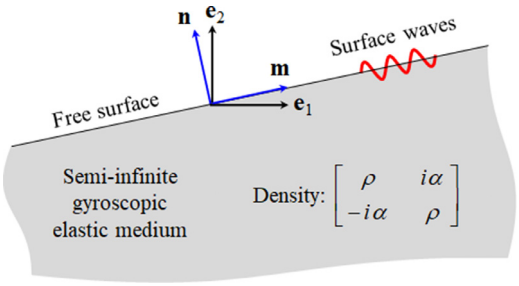

Fig. 1. The geometry of the problem for formulating surface states of a half-space gyroscopic elastic medium with the traction-free surface.

where $\mathbf{C}$ is the fourth-order elasticity tensor, ε is the infinitesimal strain tensor, which is related to the displacement $\mathbf{u}$ by $\boldsymbol{\varepsilon} = \frac{1}{2}(\mathbf{u}\nabla + \nabla\mathbf{u})$. By substitution of Eq. (3) into (1), the elastodynamic equation of the gyroscopic medium can be written in terms of the displacement as

$$\nabla \cdot (\mathbf{C} : \nabla\mathbf{u}) = \boldsymbol{\rho}\partial^2\mathbf{u}/\partial t^2. \tag{4}$$

In the Cartesian coordinate system of base vectors $\mathbf{e}_1$ and $\mathbf{e}_2$, Eq. (4) is written in the component form as

$$C_{jkrs}\frac{\partial^2 u_r}{\partial x_k \partial x_s} = \rho_{jk}\frac{\partial^2 u_k}{\partial t^2}. \tag{5}$$

Let $\mathbf{m} = m_j\mathbf{e}_j$ and $\mathbf{n} = n_j\mathbf{e}_j$ be orthogonal unit vectors. The gyroscopic medium occupies the half-space $\mathbf{n}\cdot\mathbf{x} \le 0$, where $\mathbf{x}$ is the position vector, and we seek solutions of a surface wave that propagates along the traction-free surface $\mathbf{n}\cdot\mathbf{x} = 0$. Notice that the surface wave solution would depend on the choice of the direction of the traction-free surface in the general anisotropic case. Thereby, the vectors $\mathbf{m}$ and $\mathbf{n}$ are set different from $\mathbf{e}_1$ and $\mathbf{e}_2$ in the present study.

2.2. New forms of wave equations

The general expression of displacement fields in the half-space gyroscopic medium can be expressed as

$$\mathbf{u} = \mathbf{a}e^{-i\xi(\mathbf{m}\cdot\mathbf{x} + p\mathbf{n}\cdot\mathbf{x} - vt)}, \tag{6}$$

where $\mathbf{a}$ is the unknown complex amplitude. The criterion for the existence of surface waves is the fact that the wave fields decay exponentially in the direction perpendicular to the surface such that the wave can only propagate along the interface without any decaying. Determination of the propagation velocity v of this surface wave is the main task of this study. According to this definition, the parallel wave number ξ, which is equal to ω/v, should be purely real, meanwhile, the imaginary part of the normal wave number p must be non-zero so that the wave fields could decay at a distance far away from the interface.

Differentiating twice the displacement (6) over space and time, respectively, leads to

$$\frac{\partial^2\mathbf{u}}{\partial x_k \partial x_s} = -\xi^2(m_k + pn_k)(m_s + pn_s)e^{-i\xi(\mathbf{m}\cdot\mathbf{x} + p\mathbf{n}\cdot\mathbf{x} - vt)}a_r\mathbf{e}_r, \tag{7}$$

$$\frac{\partial^2\mathbf{u}}{\partial t^2} = -\xi^2 v^2 e^{-i\xi(\mathbf{m}\cdot\mathbf{x} + p\mathbf{n}\cdot\mathbf{x} - vt)}a_r\mathbf{e}_r. \tag{8}$$

Substitution of the above equations into the wave Eq. (5) gives rise to

$$\left[C_{jkrs}(m_k + pn_k)(m_s + pn_s) - \rho_{jr}v^2\right]a_r = 0. \tag{9}$$

Expansion of Eq. (9) generates

$$\left[C_{jkrs}m_k m_s - \rho_{jr}v^2 + p\left(C_{jkrs}m_k n_s + C_{jkrs}n_k m_s\right) + p^2 C_{jkrs}n_k n_s\right]a_r = 0. \tag{10}$$

We define the first two terms in the bracket as the gyroscopic elastic coefficients, denoted by C^{gyro}_{jkrs}, which gives

$$C^{\text{gyro}}_{jkrs} = C_{jkrs} - \rho_{jr}v^2 m_k m_s. \tag{11}$$

To proceed, three matrices $\mathbf{Q}$, $\mathbf{R}$, and $\mathbf{T}$ were introduced (Tanuma, 2007)

$$[\mathbf{Q}]_{jr} = C^{\text{gyro}}_{jkrs}m_k m_s,\ [\mathbf{R}]_{jr} = C^{\text{gyro}}_{jkrs}m_k n_s,\ [\mathbf{T}]_{jr} = C^{\text{gyro}}_{jkrs}n_k n_s. \tag{12}$$

Consider the fact that $\mathbf{m}$ and $\mathbf{n}$ are unit vectors perpendicular to each other, namely $m_k m_k = 1$, $n_k n_k = 1$, and $m_k n_k = 0$. $\mathbf{Q}$, $\mathbf{R}$, and $\mathbf{T}$ can be rewritten as

$$[\mathbf{Q}]_{jr} = C_{jkrs}m_k m_s - \rho_{jr}v^2,\ [\mathbf{R}]_{jr} = C_{jkrs}m_k n_s,\ [\mathbf{T}]_{jr} = C_{jkrs}n_k n_s. \tag{13}$$

In terms of **Q**, **R**, and **T**, the wave Eq. (10) can be written in the following compacted form

$$\left[\mathbf{Q}+p\left(\mathbf{R}+\mathbf{R}^{T}\right)+p^{2}\mathbf{T}\right]\mathbf{a}=\mathbf{0}, \tag{14}$$

where the superscript "T" stands for the tensor transpose. An alternative form of Eq. (10) can be written as

$$\left[C_{jkrs}^{\mathrm{gyro}}(m_k+pn_k)(m_s+pn_s)\right]a_r=0. \tag{15}$$

For general anisotropic material, Eq. (10) leads to the quadratic eigenvalue problem with the eigenvalue p, which belongs to a nonlinear eigenproblem and is not easily solved. Besides, the presence of Hermite density ρ_{jr} adds more difficulty to the analysis of Eq. (10). Thereby, the direct computation of the eigenvalue p using Eq. (10) is very difficult. Without an explicit expression of the displacement solution, it would be also difficult to compute the surface wave velocity according to the traction free boundary conditions. To overcome the above challenges, the Stroh formalism will be adopted and significantly modified to derive analytic conditions for the existence of surface waves propagating at the traction-free boundary of a half-space gyroscopic elastic medium.

2.3. Surface state equation

The Cauchy stress vector **t** at the free surface, $\mathbf{t}=\sigma_{jk}n_k\mathbf{e}_j$, is expressed as a function of the displacement by

$$\mathbf{t}=C_{jkrs}\frac{\partial u_r}{\partial x_s}n_k\mathbf{e}_j. \tag{16}$$

Substitution of Eq. (6) into (16) results in

$$\mathbf{t}=-i\xi\left[C_{jkrs}(m_s+pn_s)n_k\right]a_r e^{-i\xi(\mathbf{m}\cdot\mathbf{x}^{s}-vt)}\mathbf{e}_j, \tag{17}$$

where $\mathbf{x}^s$ refers to the position vector of points at the free surface. With the help of Eq. (13), the interface stress vector can be written as

$$\mathbf{t}=-i\xi\mathbf{l}e^{-i\xi(\mathbf{m}\cdot\mathbf{x}^{s}-vt)}, \tag{18}$$

where **l** is the complex amplitude of the traction, given by

$$\mathbf{l}=\left(\mathbf{R}^{T}+p\mathbf{T}\right)\mathbf{a}. \tag{19}$$

Using Eq. (19), the explicit expression for $p\mathbf{a}$ is obtained as

$$p\mathbf{a}=-\mathbf{T}^{-1}\mathbf{R}^{T}\mathbf{a}+\mathbf{T}^{-1}\mathbf{l}. \tag{20}$$

Note that in Eq. (20), the matrix **T** is invertible and its inverse matrix $\mathbf{T}^{-1}$exists according to the convexity of elastic potentials (Tanuma, 2007). Eq. (20) is one of two necessary equations for formulating the surface state. To acquire the other, multiplying p on both sides of Eq. (19) produces

$$p\mathbf{l}=\left(p\mathbf{R}^{T}+p^{2}\mathbf{T}\right)\mathbf{a}. \tag{21}$$

Eq. (14) can be rewritten as $-(\mathbf{Q}+p\mathbf{R})\mathbf{a}=(p\mathbf{R}^{T}+p^{2}\mathbf{T})\mathbf{a}$, which is substituted into Eq. (21) leading to

$$p\mathbf{l}=-(\mathbf{Q}+p\mathbf{R})\mathbf{a}. \tag{22}$$

To eliminate p on the r.h.s. of Eq. (22), substituting (20) into (22) gives rise to

$$p\mathbf{l}=\left(-\mathbf{Q}+\mathbf{R}\mathbf{T}^{-1}\mathbf{R}^{T}\right)\mathbf{a}-\mathbf{R}\mathbf{T}^{-1}\mathbf{l}. \tag{23}$$

Combining Eqs. (20) and (23) leads to the final form of the Stroh's eigenvalue equation

$$\mathbf{N}\begin{bmatrix}\mathbf{a}\\ \mathbf{l}\end{bmatrix}=p\begin{bmatrix}\mathbf{a}\\ \mathbf{l}\end{bmatrix}, \tag{24}$$

where p is the eigenvalue, $[\ \mathbf{a}\quad \mathbf{l}\ ]^T$ is the eigenvector, and the 4×4 Stroh eigen-matrix **N** is defined as

$$\mathbf{N}=\begin{bmatrix}-\mathbf{T}^{-1}\mathbf{R}^{T} & \mathbf{T}^{-1}\\ -\mathbf{Q}+\mathbf{R}\mathbf{T}^{-1}\mathbf{R}^{T} & -\mathbf{R}\mathbf{T}^{-1}\end{bmatrix}. \tag{25}$$

In contrast to the quadratic eigenvalue Eq. (10), Eq. (24) leads to the linear eigenvalue problem, which is readily solved even in the presence of Hermite density.

Now recall the wave Eq. (14), which would result in the following secular equation that the eigenvalue p must satisfy

$$\det\left[\mathbf{Q}+p\left(\mathbf{R}+\mathbf{R}^{T}\right)+p^{2}\mathbf{T}\right]=0. \tag{26}$$

Taking the conjugate transpose (denoted by the superscript "*") on Eq. (26) will obtain

$$\det\left[\mathbf{Q}^{*}+\bar{p}\left(\mathbf{R}+\mathbf{R}^{T}\right)+\bar{p}^{2}\mathbf{T}^{*}\right]=0, \tag{27}$$

where the overbar denotes the conjugate operation. The matrix $\mathbf{Q}$ relates the Hermite form, satisfying $\mathbf{Q}^* = \mathbf{Q}$. Moreover, $\mathbf{T}$ is the real-valued matrix according to its definition in Eq. (13), which implies that $\mathbf{T}^* = \mathbf{T}^T$ with $[\mathbf{T}^T]_{rj} = C_{rkjs} n_k n_s$. According to the relation $C_{rkjs} = C_{jsrk}$, we further have $\mathbf{T}^T = \mathbf{T}$. Consequently, Eq. (27) can be rewritten as

$$\det\left[\mathbf{Q} + \bar{p}\left(\mathbf{R} + \mathbf{R}^T\right) + \bar{p}^2\mathbf{T}\right] = 0 \tag{28}$$

It is found by comparing Eqs. (26) and (28) that p and its conjugate $\bar{p}$ are both eigenvalues of the secular equation.

It can be deduced from the above analyses that eigenvalues of the surface wave Eq. (24) consist of two conjugate pairs, which are denoted as p_1^+ and $p_1^-(=\bar{p}_1^+)$ for one pair, p_2^+ and $p_2^-(=\bar{p}_2^+)$ for the other. Here, the superscript "+" or "-" symbol identifies the sign of the imaginary part of p and also indicates the forward or backward propagation direction of the surface waves. The associated eigenvectors are denoted by $\mathbf{a}_1^+$, $\mathbf{a}_1^-$, $\mathbf{a}_2^+$ and $\mathbf{a}_2^-$ for the displacement while $\mathbf{l}_1^+$, $\mathbf{l}_1^-$, $\mathbf{l}_2^+$ and $\mathbf{l}_2^-$ denotes the surface traction. According to Eq. (6), the modal displacement fields can be expressed explicitly as

$$\mathbf{u}_j^+ = \mathbf{a}_j^+ e^{-i\xi\left(\mathbf{m}\cdot\mathbf{x} + p_j^+\mathbf{n}\cdot\mathbf{x} - vt\right)},\ j = 1, 2, \tag{29}$$

for the surface wave traveling toward the positive $\mathbf{m}$ direction, in which $v > 0$ and $\xi = \omega/v > 0$, and

$$\mathbf{u}_j^- = \mathbf{a}_j^- e^{-i\xi\left(\mathbf{m}\cdot\mathbf{x} + p_j^-\mathbf{n}\cdot\mathbf{x} - vt\right)},\ j = 1,\ 2, \tag{30}$$

for the surface wave traveling toward the negative $\mathbf{m}$ direction with $v < 0$ and $\xi < 0$. The surface traction is expressed as

$$\mathbf{t} = \begin{cases} -i\xi c_j^+ \mathbf{l}_j^+ e^{-i\xi(\mathbf{m}\cdot\mathbf{x}^s - vt)}, v > 0 \\ -i\xi c_j^- \mathbf{l}_j^- e^{-i\xi(\mathbf{m}\cdot\mathbf{x}^s - vt)}, v < 0 \end{cases} \tag{31}$$

where c_j^+ and c_j^- are unknown coefficients. The traction-free boundary condition $\mathbf{t} = \mathbf{0}$ requires that

$$c_j^+\mathbf{l}_j^+ = \mathbf{0},\ \text{for}\, v > 0;\ c_j^-\mathbf{l}_j^- = \mathbf{0},\ \text{for}\, v < 0. \tag{32}$$

Thereby, the wave speed v can be solved from

$$det\left[\mathbf{l}_1^+, \mathbf{l}_2^+\right] = 0, \text{for}\, v > 0;\ det\left[\mathbf{l}_1^-, \mathbf{l}_2^-\right] = 0,\ \text{for}\, v < 0 \tag{33}$$

In the case of $\alpha = 0$, Eq. (25) defines the real-valued matrix $\mathbf{N}$. By imposing the conjugate operation on (24), we deduce that $\mathbf{a}_j^+$ and $\mathbf{a}_j^-$ as well as $\mathbf{l}_j^+$ and $\mathbf{l}_j^-$ are conjugate to each other. This implies that the forward ($v > 0$) and backward ($v < 0$) traveling waves possess the same mode shape, and thus implies the same velocity magnitude. If $\alpha \neq 0$, we can infer the dissimilar speeds for waves propagating in two opposite directions because the pair $\mathbf{a}_j^+$ and $\mathbf{a}_j^-$ or $\mathbf{l}_j^+$ and $\mathbf{l}_j^-$ are no longer conjugates owing to the complex operator $\mathbf{N}$.

2.4. Conditions for identifying the surface mode

The solutions of Eq. (33) contain both the surface and bulk states supported by the system. The condition for identifying a surface mode is that the imaginary part of p must be non-zero so that the wave fields could decay at a distance far away from the interface. In this section, an inequality will be given to identify a wave velocity range corresponding to the surface mode, within which the imaginary parts of the associated eigenvalues p are non-zero.

Introduce two orthogonal unit vectors $\tilde{\mathbf{m}}$ and $\tilde{\mathbf{n}}$, which are obtained by rotating the unit vectors $\mathbf{m}$ and $\mathbf{n}$ around the coordinate origin by an angle ϕ ($-\pi \le \phi < \pi$). The vectors $\tilde{\mathbf{m}}$ and $\tilde{\mathbf{n}}$ are written as a function of ϕ by (Tanuma, 2007)

$$\tilde{\mathbf{m}}(\phi) = \mathbf{m}\cos\phi + \mathbf{n}\sin\phi,\ \tilde{\mathbf{n}}(\phi) = -\mathbf{m}\sin\phi + \mathbf{n}\cos\phi \tag{34}$$

We define the Hermitian matrix $\tilde{\mathbf{Q}}(\phi)$ as

$$\left[\tilde{\mathbf{Q}}(\phi)\right]_{jr} = C_{jkrs}\tilde{m}_k\tilde{m}_s - \rho_{jr}v^2\cos^2\phi \tag{35}$$

Notice that $\tilde{\mathbf{Q}}(0)$ is equal to $\mathbf{Q}$ in Eq. (13). Two real eigenvalues, which are denoted as $q_1(\phi)$ and $q_2(\phi)$, can be solved from the 2×2 Hermitian matrix $\tilde{\mathbf{Q}}(\phi)$. We claim that the condition for identifying the surface mode is that the matrix $\tilde{\mathbf{Q}}(\phi)$ is positive definite, namely $q_1(\phi)$,$q_2(\phi) > 0$, for any ϕ. In other words, if $\tilde{\mathbf{Q}}(\phi)$ is positive definite for the wave velocity v of a mode, the eigenvalue p would surely possess a non-zero imaginary part and corresponds to a surface mode, as demonstrated below.

We first examine the case that $\det\tilde{\mathbf{Q}}(\phi) = 0$. When $\cos\phi \neq 0$, $\tilde{\mathbf{Q}}(\phi)$ is written in terms of $\mathbf{Q}$, $\mathbf{R}$ and $\mathbf{T}$ as

$$\tilde{\mathbf{Q}}(\phi) = \cos^2\phi\left[\mathbf{Q} + \tan\phi\left(\mathbf{R} + \mathbf{R}^T\right) + \tan^2\phi\mathbf{T}\right] \tag{36}$$

If $\det\tilde{\mathbf{Q}}(\phi) = 0$, it can be obtained from Eq. (36) that

$$\det\left[\mathbf{Q} + \tan\phi\left(\mathbf{R} + \mathbf{R}^T\right) + \tan^2\phi\mathbf{T}\right] = 0 \tag{37}$$

By comparing Eqs. (14) and (37), the real-valued eigenvalue $p = \tan\phi$ can be found, indicating that $\det\tilde{\mathbf{Q}}(\phi) = 0$ doesn't correspond to a surface mode. Notice that $\det\tilde{\mathbf{Q}}(\phi) = 0$ cannot appear under a special angle $\phi = \phi_+$ with $\cos\phi_+ = 0$, because $\tilde{\mathbf{Q}}(\phi_+) = \mathbf{T}$, where $\mathbf{T}$ is always positive definite as a result of the convexity of elastic potential energy. We next consider the

case that $\det\tilde{\mathbf{Q}}(\phi) < 0$. Assume that ϕ_- is an angle satisfying $\det\tilde{\mathbf{Q}}(\phi_-) < 0$. Recall that $\det\tilde{\mathbf{Q}}(\phi_+) > 0$ holds for the angle ϕ_+ that satisfies $\cos\phi_+ = 0$. Owing to the fact that $\det\tilde{\mathbf{Q}}(\phi)$ is a continuous function of ϕ in the interval from $-\pi$ to π, one can always determine an angle ϕ_0 such that $\det\tilde{\mathbf{Q}}(\phi_0) = 0$. However, $\det\tilde{\mathbf{Q}}(\phi_0) = 0$ would result in a real-valued p, as demonstrated previously. Thereby, $\det\tilde{\mathbf{Q}}(\phi) < 0$ doesn't also correspond to a surface mode. Based on the above analysis, we conclude that the condition for identifying the surface mode is given by $\det\tilde{\mathbf{Q}}(\phi) > 0$, or equivalently

$$q_1(\phi), q_2(\phi) > 0 \text{ for any } \phi \tag{38}$$

It is noteworthy that the presence of a real-valued eigenvalue p is excluded by the condition (38). To explain this, assume that there exists a real-valued eigenvalue p under condition (38). For an arbitrary real value $p \in \mathbb{R}$, one can always define an angle ϕ that satisfies $p = \tan\phi$, so that Eqs. (14) and (37) are identical. Then we can obtain $\det\tilde{\mathbf{Q}}(\phi) = 0$ from Eq. (36), which however contradicts with the condition (38).

3. Non-reciprocal Rayleigh waves in the isotropic case

In this section, the surface state equation and the condition for identifying the surface mode are given for continuum materials with isotropic elasticity and chiral density. Numerical examples are provided to illustrate the non-reciprocal behaviors of Rayleigh surface waves.

3.1. Surface state equation

In the isotropic case, the elasticity tensor C_{jkrs} is given by

$$C_{jkrs} = \lambda\delta_{jk}\delta_{rs} + \mu\left(\delta_{jr}\delta_{ks} + \delta_{js}\delta_{rk}\right) \tag{39}$$

where δ_{jk} is Kronecker's delta, and λ, μ are the Lamé constants. The matrices **Q**, **R**, and **T** in Eq. (13) are simplified as

$$\mathbf{Q} = \begin{bmatrix} \lambda + 2\mu - \rho v^2 & -i\alpha v^2 \\ i\alpha v^2 & \mu - \rho v^2 \end{bmatrix}, \ \mathbf{R} = \begin{bmatrix} 0 & \lambda \\ \mu & 0 \end{bmatrix}, \ \mathbf{T} = \begin{bmatrix} \mu & 0 \\ 0 & \lambda + 2\mu \end{bmatrix}. \tag{40}$$

It can be verified that three matrices in Eq. (40) are isotropic, retaining the invariant form with the rotation of coordinates. The Stroh eigen-matrix **N** defined by Eq. (25) is expressed as

$$\mathbf{N} = \begin{bmatrix} 0 & -1 & \frac{1}{\mu} & 0 \\ -\frac{\lambda}{\lambda+2\mu} & 0 & 0 & \frac{1}{\lambda+2\mu} \\ \rho v^2 - \frac{4\lambda\mu+4\mu^2}{\lambda+2\mu} & i\alpha v^2 & 0 & -\frac{\lambda}{\lambda+2\mu} \\ -i\alpha v^2 & \rho v^2 & -1 & 0 \end{bmatrix} \tag{41}$$

Solving the matrix **N** for the eigenvalue p to generate

$$p_1^{\pm} = \pm i\sqrt{1 - \frac{(\lambda+3\mu)\rho v^2 + \sqrt{(\lambda+\mu)^2\rho^2 v^4 + 4\mu(\lambda+2\mu)\alpha^2 v^4}}{2\mu(\lambda+2\mu)}} \tag{42}$$

$$p_2^{\pm} = \pm i\sqrt{1 - \frac{(\lambda+3\mu)\rho v^2 - \sqrt{(\lambda+\mu)^2\rho^2 v^4 + 4\mu(\lambda+2\mu)\alpha^2 v^4}}{2\mu(\lambda+2\mu)}} \tag{43}$$

The corresponding traction part of eigenvectors can be determined according to Eq. (24), producing

$$\mathbf{l}_1^{\pm} = \begin{bmatrix} \mu p_1^{\pm}\beta_1^{\pm} + \mu \\ \lambda\beta_1^{\pm} + (\lambda+2\mu)p_1^{\pm} \end{bmatrix}, \ \mathbf{l}_2^{\pm} = \begin{bmatrix} \mu p_2^{\pm}\beta_2^{\pm} + \mu \\ \lambda\beta_2^{\pm} + (\lambda+2\mu)p_2^{\pm} \end{bmatrix}, \tag{44}$$

where

$$\beta_1^{\pm} = \frac{(\lambda+\mu)\left[1 - \left(p_1^{\pm}\right)^2\right] - \sqrt{(\lambda+\mu)^2\left[1 + \left(p_1^{\pm}\right)^2\right]^2 + 4\alpha^2 v^4}}{2p_1^{\pm}(\lambda+\mu) + 2i\alpha v^2}, \tag{45}$$

$$\beta_2^{\pm} = \frac{(\lambda+\mu)\left[1 - \left(p_2^{\pm}\right)^2\right] + \sqrt{(\lambda+\mu)^2\left[1 + \left(p_2^{\pm}\right)^2\right]^2 + 4\alpha^2 v^4}}{2p_2^{\pm}(\lambda+\mu) + 2i\alpha v^2}. \tag{46}$$

Substituting Eq. (44) into (33) results in the following equation that determine the surface wave velocity

$$\frac{\beta_1^+\beta_2^+\left(p_1^+ - p_2^+\right) + \beta_2^+ - \beta_1^+}{\left(p_1^+ - p_2^+\right) + p_1^+p_2^+\left(\beta_2^+ - \beta_1^+\right)} = 1 + 2\frac{\mu}{\lambda}, \text{ for } v > 0 \tag{47}$$

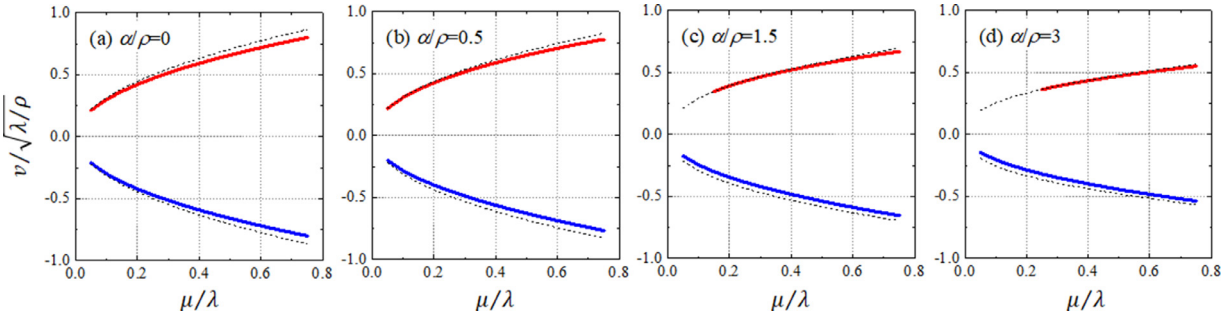

Fig. 2. The surface wave velocity v (solid line) and cutoff velocity v_c (dashed line) for different values of μ/λ in four cases α/ρ=0 (a), 0.5 (b), 1.5 (c), and 3 (d). The used material parameters are λ=10 GPa and ρ=1000 kg/m^3.

$$\frac{\beta_1^-\beta_2^-\left(p_1^- - p_2^-\right) + \beta_2^- - \beta_1^-}{\left(p_1^- - p_2^-\right) + p_1^- p_2^-\left(\beta_2^- - \beta_1^-\right)} = 1 + 2\frac{\mu}{\lambda},\ \text{for},\ v < 0 \tag{48}$$

When $\alpha = 0$, we have $\beta_j^+ = -\beta_j^-$ and $p_j^+ = -p_j^-$, thus the two Eqs. (47) and (48) are identical, giving rise to the surface wave speed irrelevant to the traveling direction. When $\alpha \neq 0$, Eqs. (47) and (48) would lead to different velocity magnitudes of forward and backward waves.

Below is an analysis of the condition for identifying the surface mode in the isotropic case. The matrix $\tilde{\mathbf{Q}}(\phi)$ as defined in Eq. (36) is simplified as

$$\tilde{\mathbf{Q}}(\phi) = \begin{bmatrix} (\lambda+\mu)\cos^2\phi + \mu & (\lambda+\mu)\cos\phi\sin\phi \\ (\lambda+\mu)\cos\phi\sin\phi & (\lambda+\mu)\sin^2\phi + \mu \end{bmatrix} - v^2\cos^2\phi \begin{bmatrix} \rho & i\alpha \\ -i\alpha & \rho \end{bmatrix}. \tag{49}$$

The eigenvalues $q_1(\phi)$ and $q_2(\phi)$ of $\tilde{\mathbf{Q}}(\phi)$ can be solved with the analytic expression

$$q_1(\phi) = \frac{1}{2}\left[\lambda + 3\mu - 2\rho v^2\cos^2\phi - \sqrt{(\lambda+\mu)^2 + 4\alpha^2 v^4\cos^4\phi}\right], \tag{50}$$

$$q_2(\phi) = \frac{1}{2}\left[\lambda + 3\mu - 2\rho v^2\cos^2\phi + \sqrt{(\lambda+\mu)^2 + 4\alpha^2 v^4\cos^4\phi}\right]. \tag{51}$$

Since $q_1(\phi) < q_2(\phi)$, the condition (38) can be expressed as $q_1(\phi) > 0$, which results in

$$|v| < \frac{v_c}{|\cos\phi|},\ \text{for any}\ \phi \tag{52}$$

where v_c is defined as the cutoff velocity, given by

$$v_c = \sqrt{\frac{2\mu(\lambda+2\mu)}{(\lambda+3\mu)\rho + \sqrt{(\lambda+\mu)^2\rho^2 + 4\mu(\lambda+2\mu)\alpha^2}}} \tag{53}$$

According to Eq. (52), the condition for identifying the surface mode is finally given by $v < v_c$. In the non-gyro case ($\alpha = 0$), we obtain that $v_c = \sqrt{\mu/\rho}$. Then the condition $v < v_c$ is reduced to $v < \sqrt{\mu/\rho}$, which is the well-known subsonic range of Rayleigh wave velocity in conventional isotropic solids.

3.2. Numerical results and discussions

In this subsection, we discuss using numerical examples the surface state solution of the gyroscopic material system. Specifically, we simulate the surface wave response of the semi-infinite gyroscopic medium subject to the point load at the free surface to investigate the propagation characteristics of non-reciprocal Rayleigh waves.

Fig. 2 shows the surface wave velocity v and the cutoff velocity v_c for different values of μ/λ in four cases α/ρ=0, 0.5, 1.5, and 3, where material parameters λ=10 GPa and ρ=1000 kg/m^3 are used. When there is no chiral coupling (α=0), the velocities are exactly the same for Rayleigh waves traveling in two opposite directions. When α/ρ=0.5, the surface wave with the positive v tends to travel faster compared to the wave toward the opposite direction, giving rise to the asymmetric wave propagation phenomenon. When α/ρ is increased to 1.5, the speed of the right-traveling surface wave exceeds the cutoff value v_c in the region of the relatively small μ/λ. The surface state relevant to this regime then disappears, leading to one-way Rayleigh waves. When α/ρ=3, the region of the unidirectional surface state increases.

In order to better understand the non-reciprocal surface waves, we compute the wave response of gyroscopic elastic medium by numerical simulations based on COMSOL Multiphysics. The gyroscopic elastic medium is modeled as a rectangle,

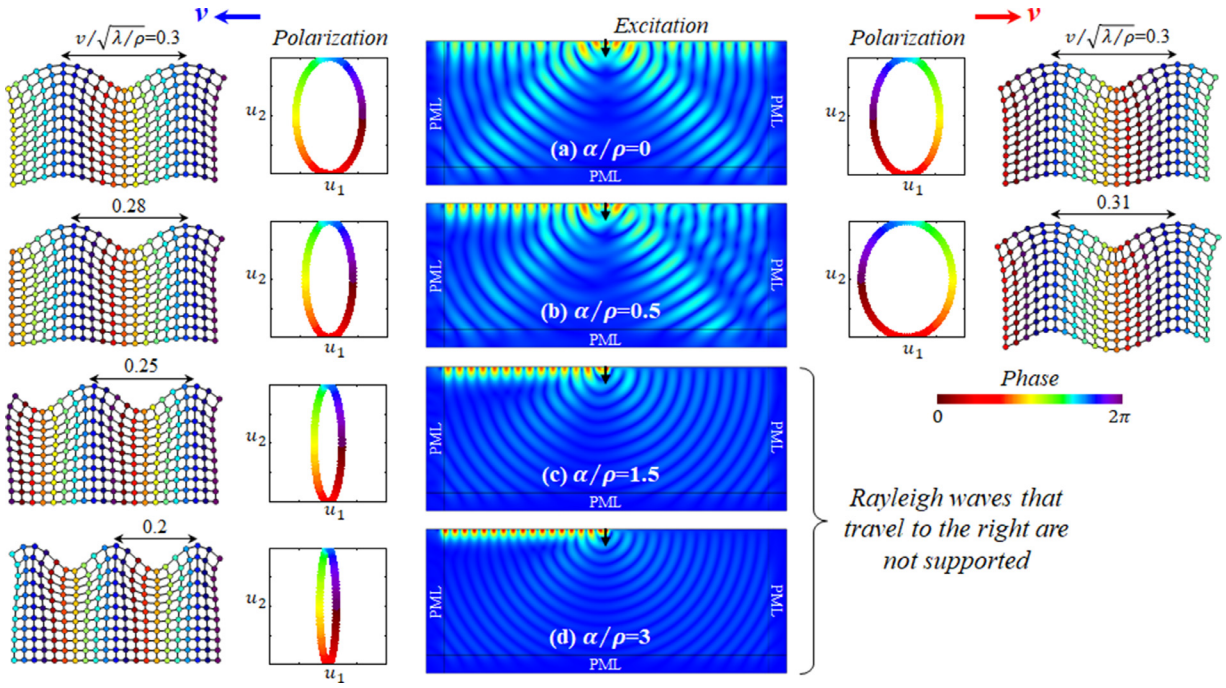

Fig. 3. The wave response of gyroscopic elastic medium subject to a time-harmonic displacement of the frequency 6 kHz at the central point of the free surface, whose direction is represented by an arrow. The simulation results (a-d) correspond to the four cases studied in Fig. 2 where μ/λ=0.1 is chosen. The particle motion trajectory at shallow depths and polarization chart of the surface displacement are illustrated for the wave traveling to the left and right.

in which the top boundary is the free surface and other boundaries are terminated by perfectly matched layers (PMLs) to eliminate unwanted reflections. At the central point of the free surface, we impose a time-harmonic displacement of frequency 6 kHz, whose direction is represented by an arrow. Choosing μ/λ=0.1 and the same material parameters used in Fig. 2, the computed scattering displacement fields shown in Fig. 3(a-d) possess four cases of α/ρ=0, 0.5, 1.5, and 3, respectively. To focus on the excited surface waves near the edge, we also plot in Fig. 3 the particle motion trajectory and the polarization chart of surface displacements for the left- and right-traveling waves. In the non-chiral case (α/ρ=0), the responses of surface waves propagating in two opposite directions are exactly symmetric. It is evident that the particle motion follows an elliptical trajectory, and the motion is counterclockwise for waves traveling toward the right, and vice versa, in agreement with previous findings (Rayleigh, 1885). When α/ρ=0.5, different polarization modes and displacement responses at shallow depths in the two opposite directions are observed. The wave traveling to the right possesses a higher velocity, meanwhile, the polarization ellipse is elongated horizontally. On the contrary, the wave to the left is slowed down in speed and the polarization ellipse is shortened horizontally. The unidirectional surface state occurs in cases of α/ρ=1.5 and 3, where Rayleigh waves that travel to the right are no longer supported. In this scenario, the speed of waves traveling to the left is further lowered and the polarization tends to become the transverse mode (i.e., the mode of vertical oscillations of particles).

4. Homogenization method of gyroscopic composite materials

The theory presented above could be used to derive the material parameters required for achieving the non-reciprocal Rayleigh wave. To realize the microstructure design of gyroscopic solids that meets the parameter requirement, the homogenization method for gyroscopic solids with the chiral inertial coupling must be established. However, it has never been proposed previously. In this section, a generic homogenization method is proposed for retrieving all effective material parameters of gyroscopic composite materials. Effective stiffnesses and chiral densities will be provided for the lattice structure consisting of gyroscopic cylinders embedded in an elastic matrix. Additionally, micromechanics based models are used for predicting effective properties in the long-wavelength limit, which are compared with the results of the developed method.

4.1. Dispersion analyses of gyroscopic composite materials

The composite structure under study is composed of a triangular lattice of cylindrical rigid body embedded into an elastic solid. To obtain the chiral effect of the inertial motion (Brun et al., 2012; Carta et al., 2014), each rigid cylinder is connected to a spinning gyroscope whose axis is perpendicular to the lattice plane, as schematically shown in Fig. 4. Consider that the

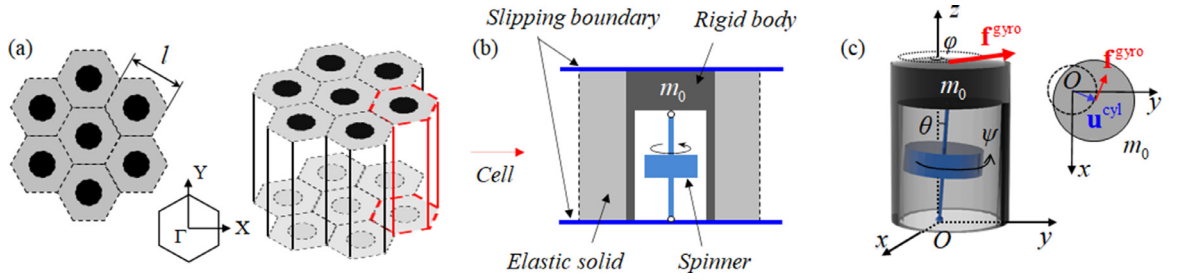

Fig. 4. Gyroscopic composite materials: (a) Schematic of the triangular lattice of cylindrical rigid body embedded into an elastic solid; (b) Geometry of unit cell. The slipping boundary condition (with the motion constrained in the *z*-direction, while free in the *x*-*y* plane) is imposed on both top and bottom surfaces to ensure that the plane strain state is followed. (c) Side and top view of rigid body inclusion in a state of motion. Each rigid cylinder is connected to a spinning gyroscope whose bottom end is pin connected to the ground.

periodic structure is of finite thickness, and the slipping boundary condition is imposed on both top and bottom surfaces. Under this condition, the composite structure could follow the plane strain state. Assume that the rigid cylinder of weight m_0 undergoes the displacement $\mathbf{u}^{cyl}$ when subjected to the external force $\mathbf{f}^{ext}$ from the matrix material. In the harmonic case, the equilibrium equation of the rigid cylinder can be expressed as

$$\mathbf{f}^{ext} + \mathbf{f}^{gyro} = -m_0\omega^2\mathbf{u}^{cyl} \tag{54}$$

wherein $\mathbf{f}^{gyro}$ represents the inertial force exerted by the spinner and satisfies $\mathbf{u}^{cyl} \cdot \mathbf{f}^{gyro} = 0$. The conservation of angular momentum of the spinner gives rise to (Brun et al., 2012; Carta et al., 2014)

$$\mathbf{u}^{cyl} \times \mathbf{f}^{gyro} = -i\omega^2 h^{-2} I_{zz} \left|\mathbf{u}^{cyl}\right|^2 \mathbf{e}_z \tag{55}$$

where I_{zz} denotes the moment of inertia about the *z*-axis and h is the characteristic length of the spinner. The following relations can be generalized from Eq. (55)

$$\mathbf{f}^{gyro} = h^{-2} I_{zz}\omega^2 \begin{bmatrix} 0 & i \\ -i & 0 \end{bmatrix} \mathbf{u}^{cyl} \tag{56}$$

By substituting (56) into (54), the explicit relation between $\mathbf{u}^{cyl}$ and $\mathbf{f}^{ext}$ can be determined

$$\mathbf{f}^{ext} = -\omega^2 \mathbf{m}_{eff} \mathbf{u}^{cyl} \tag{57}$$

with

$$\mathbf{m}_{eff} = \begin{bmatrix} m_0 & ih^{-2}I_{zz} \\ -ih^{-2}I_{zz} & m_0 \end{bmatrix} \tag{58}$$

It is shown in Eq. (57) that the rigid cylinder with the loaded gyroscope can be effectively represented by a homogeneous body with effective mass $\mathbf{m}_{eff}$ that follows the tensor form of Eq. (58). To simplify the theoretical analysis, the cylindrical inclusion loaded with gyros is modeled as a homogeneous material whose mass density $\boldsymbol{\rho}_1 = [(\rho_1, i\alpha_1), (-i\alpha_1, \rho_1)]$ is set in accordance with the form of Eq. (58), herein the spinner constant α_1 is a parameter relevant to the characteristic length h and moment of inertia I_{zz} of the gyroscope. The Young's modulus, Poisson's ratio, density are taken respectively as $E_1 = 195$ GPa, $\nu_1 = 0.28$, and ρ_1=7700 kg/m^3 for the inclusion, and $E_0 = 2$ GPa, $\nu_0 = 0.41$, and ρ_0=1100 kg/m^3 for the matrix material. The inclusion's diameter is set as 1 cm, and the lattice periodicity is chosen as l=$\sqrt{3}$ cm.

The effective-medium method is developed based on the band structure results. For this purpose, we first examine the band diagram of the gyroscopic structure with different spinner constants. Fig. 5(a) shows the dispersion diagram of the composite material with α_1=0, which is computed in the ΓX and ΓY direction of the first Brillion zone. The high and low branches in the two directions correspond to the longitudinal (L) and transverse (T) polarization states, respectively, as can be easily recognized by the mode shapes at the frequency 5 kHz in Fig. 5(b). When α_1=ρ_1, two dispersion branches are still observed [Fig. 5(d)], but it is deduced from the modal displacement field in Fig. 5(e) that the particle motion now follows the elliptical trajectory as a result of the chiral coupling between the horizontal and vertical oscillation of inclusions. To highlight this difference, the high and low dispersion branches in the case of $\alpha_1 \neq 0$ are denoted by the quasi-longitudinal (QL) and quasi-transverse (QT) modes, respectively.

When the spinner constant takes the larger value, $\alpha_1 = 6\rho_1$, it is deduced that the QT mode still exists, while the QL branch disappears (Fig. 5g). This single-mode behavior can be mathematically explained by analyzing the phase velocity v_{QL} and v_{QT} of the respective QL and QT waves in the gyroscopic continuum, which can be derived by the Stroh method as

$$v_{QL} = \sqrt{\frac{2\mu(\lambda+2\mu)}{(\lambda+3\mu)\rho - \sqrt{(\lambda+\mu)^2\rho^2 + 4\mu(\lambda+2\mu)\alpha^2}}} \tag{59}$$

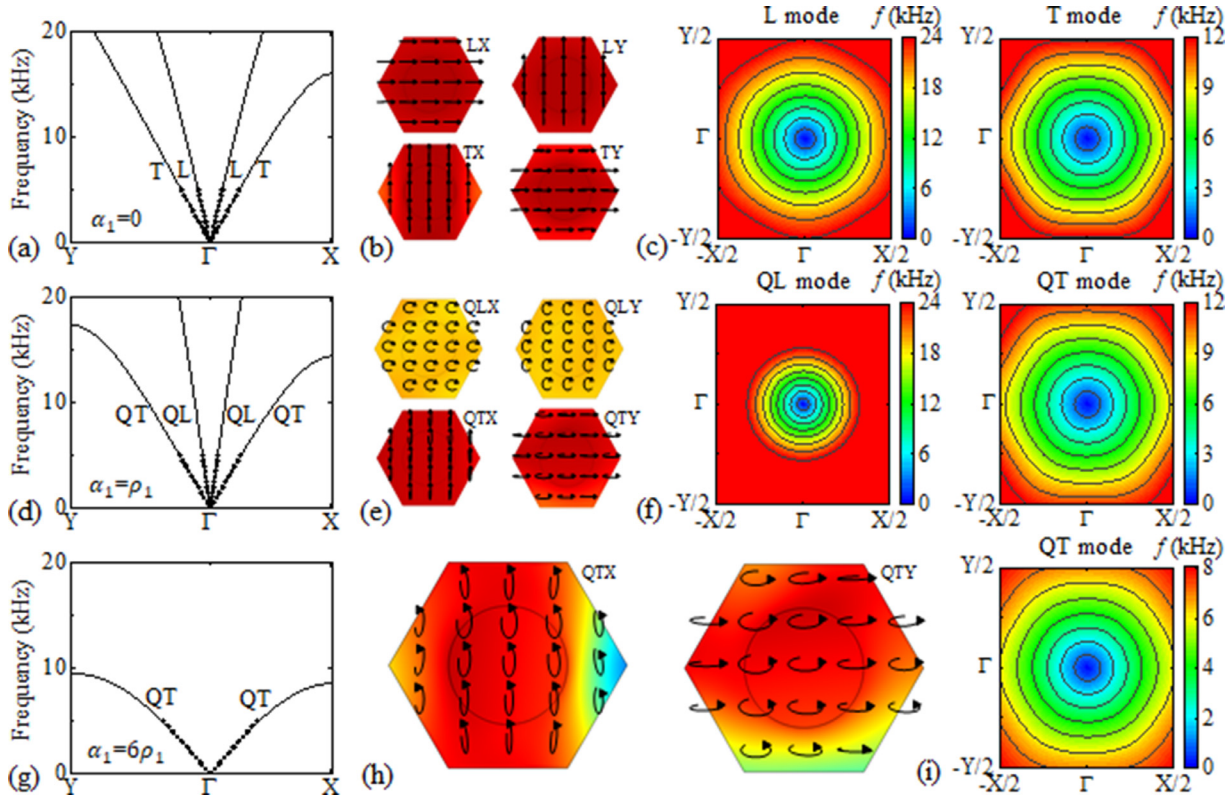

Fig. 5. The dispersion diagram of composite materials with (a) α_1=0, (d) α_1=ρ_1, and (g) α_1= 6ρ_1, calculated in the ΓX and ΓY direction of the first Brillion zone. (b,e,h) The modal displacement fields at the frequency 5 kHz for each polarization mode. (c,f,i) The isofrequency contour for the composites with different spinner constants.

$$v_{\mathrm{QT}} = \sqrt{\frac{2\mu(\lambda+2\mu)}{(\lambda+3\mu)\rho+\sqrt{(\lambda+\mu)^2\rho^2+4\mu(\lambda+2\mu)\alpha^2}}} \tag{60}$$

Note that v_{QT} has the same expression as the cutoff velocity v_{c} in Eq. (53). For the continuum medium that is characterized by $\alpha > \rho$, it is shown from Eq. (59) that v_{QL} is purely imaginary, corresponding to the stopband of the QL mode, while the QT mode exists since v_{QT} is always real. As later demonstrated by the homogenization results in Fig. 6(c) that the composite material with the spinner constant α_1= 6ρ_1 has the effective property that satisfies $\alpha > \rho$. Therefore, the QL branch is absent in the dispersion diagram (Fig. 5g).

We also calculate the isofrequency contour for the composites with different spinner constants as shown in Fig. 5(c,f,i). The nearly circular isofrequency line is observed in the vicinity of the Γ point, which demonstrates the isotropic wave behavior of the periodic composite.

4.2. Homogenization method of gyroscopic composite materials

The geometry of a triangular lattice possesses two mutually perpendicular planes of symmetry consistent with the ΓX and ΓY directions, which correspond to orthotropic material properties. So, the homogenization relations of gyroscopic composite materials are described by the elastodynamic equation with the orthotropic elasticity and tensorial density. The constitutive equation that governs the orthotropic elasticity is given by

$$\begin{bmatrix}\sigma_{xx}\\ \sigma_{yy}\\ \sigma_{xy}\end{bmatrix} = \begin{bmatrix}c_{11} & c_{12} & 0\\ c_{21} & c_{22} & 0\\ 0 & 0 & c_{44}\end{bmatrix}\begin{bmatrix}\varepsilon_{xx}\\ \varepsilon_{yy}\\ 2\varepsilon_{xy}\end{bmatrix} \tag{61}$$

To retrieve effective constitutive parameters, i.e., c_{11}, c_{12}, c_{21}, c_{22}, and c_{44}, the stress $\sigma_{\alpha\beta}$ and strain $\varepsilon_{\alpha\beta}$ (α,β=x or y) are obtained by averaging the local modal fields over a single cell (Cheng et al., 2017; Liu et al., 2011). Recall that in the non-gyro case (Cheng et al., 2017) the average normal stress and strain are obtained from the L mode in both ΓX and ΓY

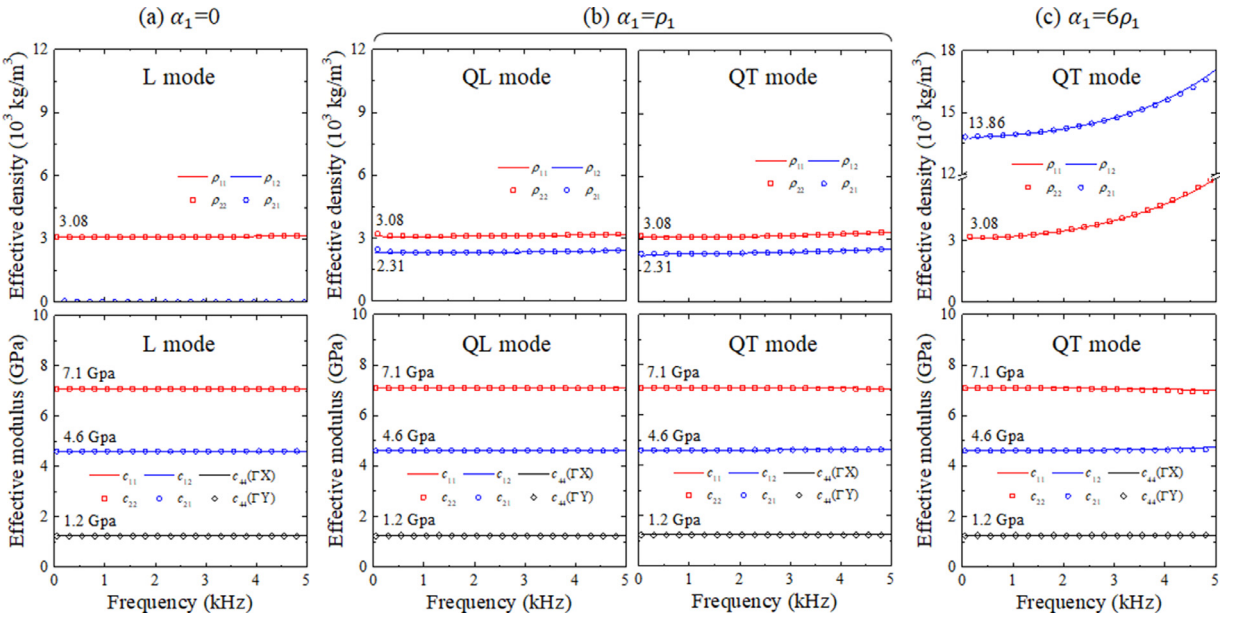

Fig. 6. Effective stiffness and density calculated for three types of composite materials with (a) α_1=0, (b) α_1=ρ_1, and (c) α_1= 6ρ_1. Especially for the composite with $\alpha_1 = \rho_1$, effective properties computed respectively from QL and QT dispersion modes are both given.

directions. Thereby, the elastic constants c_{11}, c_{12}, c_{21}, and c_{22} are determined by solving the following set of equations

$$\begin{bmatrix} \langle\sigma_{xx}\rangle_{\mathrm{LX}} \\ \langle\sigma_{yy}\rangle_{\mathrm{LX}} \\ \langle\sigma_{xx}\rangle_{\mathrm{LY}} \\ \langle\sigma_{yy}\rangle_{\mathrm{LY}} \end{bmatrix} = \begin{bmatrix} c_{11} & c_{12} & \mathbf{0} & \\ c_{21} & c_{22} & & \\ & \mathbf{0} & c_{11} & c_{12} \\ & & c_{21} & c_{22} \end{bmatrix} \begin{bmatrix} \langle\varepsilon_{xx}\rangle_{\mathrm{LX}} \\ \langle\varepsilon_{yy}\rangle_{\mathrm{LX}} \\ \langle\varepsilon_{xx}\rangle_{\mathrm{LY}} \\ \langle\varepsilon_{yy}\rangle_{\mathrm{LY}} \end{bmatrix}, \tag{62}$$

where $\langle\ \cdot\ \rangle$ denotes the averaging quantity. The average shear stress and strain are attained from the T branch that is characterized by the pure shear motion. So, the shear stiffness c_{44} can be estimated by the equation

$$\langle\sigma_{xy}\rangle_{\mathrm{TX}} = 2c_{44}\langle\varepsilon_{xy}\rangle_{\mathrm{TX}},\ \text{or}\langle\sigma_{yx}\rangle_{\mathrm{TY}} = 2c_{44}\langle\varepsilon_{yx}\rangle_{\mathrm{TY}}. \tag{63}$$

In contrast, the QL and QT dispersion branches displayed by the gyroscopic medium couple both longitudinal and transverse motions as illustrated in Fig. 5. Therefore, the average of the stress and strain is defined from either QL or QT branch. This significant extension of the effective method makes it possible to retrieve all homogenization parameters of the gyroscopic materials from single QL or QT modal fields. For example, the shear stiffness, which was usually retrieved from the transverse model for conventional solids, could be determined from either QL or QT mode for gyroscopic materials. On the other hand, the macroscopic equation of inertial motion with the tensorial density follows from

$$\begin{bmatrix} F_x \\ F_y \end{bmatrix} = \begin{bmatrix} \rho_{11} & i\rho_{12} \\ -i\rho_{21} & \rho_{22} \end{bmatrix} \begin{bmatrix} \ddot{U}_x \\ \ddot{U}_y \end{bmatrix} \tag{64}$$

where the net force $\mathbf{F}$ and acceleration $\ddot{\mathbf{U}}$ are obtained by averaging the local fields over the elementary cell (Cheng et al., 2017; Liu et al., 2011). By establishing the set of equations relevant to the QL or QT branch in both ΓX and ΓY directions, all density parameters can be determined from

$$\begin{bmatrix} \langle F_x\rangle_{\Gamma\mathrm{X}} \\ \langle F_y\rangle_{\Gamma\mathrm{X}} \\ \langle F_x\rangle_{\Gamma\mathrm{Y}} \\ \langle F_y\rangle_{\Gamma\mathrm{Y}} \end{bmatrix} = \begin{bmatrix} \rho_{11} & i\rho_{12} & \mathbf{0} & \\ -i\rho_{21} & \rho_{22} & & \\ & \mathbf{0} & \rho_{11} & i\rho_{12} \\ & & -i\rho_{21} & \rho_{22} \end{bmatrix} \begin{bmatrix} \langle\ddot{U}_x\rangle_{\Gamma\mathrm{X}} \\ \langle\ddot{U}_y\rangle_{\Gamma\mathrm{X}} \\ \langle\ddot{U}_x\rangle_{\Gamma\mathrm{Y}} \\ \langle\ddot{U}_y\rangle_{\Gamma\mathrm{Y}} \end{bmatrix} \tag{65}$$

Fig. 6 shows the effective properties calculated for three types of composite materials studied in Fig. 5 that have different spinner constants α_1=0, ρ_1, and 6ρ_1. Note that for the case of $\alpha_1 = \rho_1$, effective properties are computed respectively from QL and QT dispersion branches and are both shown in Fig. 6(b), and the excellent agreement between these two results can be verified. Comparing Fig. 6(a,b,c), we observe the relation of $\rho_{11} = \rho_{22}$ and $c_{11} = c_{22}$, which verifies the isotropic behavior. It is found that the diagonal density is equal to the volume-averaged one at the quasistatic limit given by $\rho_0 c_0 + \rho_1 c_1 \approx 3080$ kg/m^3, where c_0 and c_1 denote the volume fraction of the matrix and inclusion, respectively. Besides, the effective spinner

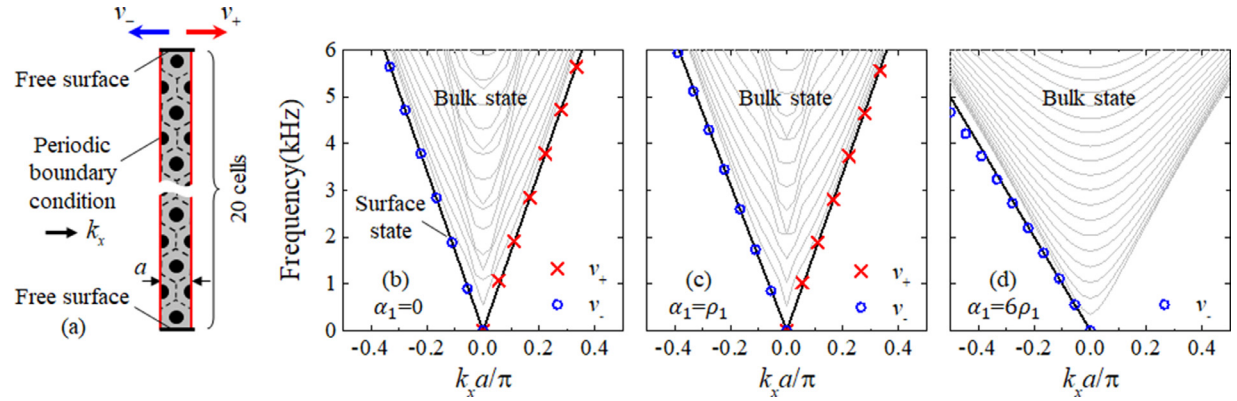

Fig. 7. (a) Sketch of the supercell consisting of 20 elementary cells arranged periodically along the vertical direction. The periodic boundary condition is applied to the direction parallel to the free surface (the top and bottom edges). (b,c,d) The computed dispersion results of bulk states (gray line) and surface states (symbol) linked to the top surface for composite materials with different spinner constants $\alpha_1 = 0$, $\alpha_1 = \rho_1$, and $\alpha_1 = 6\rho_1$. The effective-medium predictions of surface modes are shown by the dark line.

constant, ρ_{12} and ρ_{21}, also follows from the volume average law given by $0c_0 + \alpha_1 c_1$ in the long-wavelength limit, which is calculated as 2310 kg/m^3 when $\alpha_1 = \rho_1$, and 13,860 kg/m^3 when $\alpha_1 = 6\rho_1$.

Effective stiffnesses in the non-gyro case (Fig. 6a) are kept nearly constant in the frequency range of interest. The non-dispersive behavior of the effective stiffnesses remains stable even when the gyroscopic coupling $\alpha_1 = \rho_1$ and $\alpha_1 = 6\rho_1$ is introduced (Fig. 6b,c), proofing the decoupling between the overall deformation and spinner's motion. This then allows us to analytically predict the effective elastic properties of the gyroscopic composites based on the Mori-Tanaka micromechanical method (Mori and Tanaka, 1973), which was suitable for the homogenization of the particulate composite with the macroscopically isotropic property. Following the Mori-Tanaka model, effective bulk and shear modulus, K_{eff} and G_{eff}, are given by

$$K_{\text{eff}} = K_0 + \frac{1}{3}G_0 + \frac{(4G_0 + 3K_0)(G_1 - G_0 + 3K_1 - 3K_0)}{3[(3 + c_1)G_0 + c_0 G_1 + 3(c_1 K_0 + c_0 K_1)]}c_1 \tag{66}$$

$$G_{\text{eff}} = G_0 + \frac{c_1}{\frac{1}{G_1 - G_0} + \frac{c_0(7G_0 + 3K_0)}{2G_0(4G_0 + 3K_0)}} \tag{67}$$

where K_j, G_j are respectively the bulk and shear modulus for the matrix ($j = 0$) and inclusion ($j = 1$). It can be computed from Eqs. (66) and (67) that, $c_{11} = K_{\text{eff}} + G_{\text{eff}} \approx 7.1$GPa, $c_{12} = K_{\text{eff}} - G_{\text{eff}} \approx 4.6$ GPa, and $c_{44} = G_{\text{eff}} \approx 1.2$GPa, which coincide very well with the effective elastic parameters computed with the developed method as shown in Fig. 6. Finally, we calculate the dispersion curves of the continuum medium having the retrieved effective parameters, which are plotted by the solid circle in Fig. 5(a,d,g). The excellent agreement of the dispersion results between the continuum and composite materials is deduced, which validates the proposed homogenization method.

4.3. Non-reciprocal Rayleigh waves in continuum and structured materials

Now, we examine the surface states of gyroscopic composites by calculating the band structure of the supercell consisting of 20 cells arranged periodically along the vertical direction. The periodic boundary condition with the Bloch wave vector k_x is applied to the direction parallel to the free surface, as shown in Fig. 7a. The computed dispersion results of bulk states together with surface states linked to the top surface are illustrated in Fig. 7b,c,d for the composites with spinner constants $\alpha_1 = 0$, $\alpha_1 = \rho_1$, and $\alpha_1 = 6\rho_1$, respectively. The branch that falls below bulk states (gray lines) represents the surface wave, which possesses the higher k_x than that of the bulk wave, as marked by the symbol. In the case of $\alpha_1 = 0$, it is seen from Fig. 7b that the dispersion curves of surface modes are symmetric with the same secant slope as guaranteed by the reciprocity principle. When $\alpha_1 = \rho_1$, asymmetric dispersion branches of surface states can be observed in two opposite directions of the wave vector space (Fig. 7c). When $\alpha_1 = 6\rho_1$, the composite structure supports only the one-way Rayleigh wave that propagates to the left (Fig. 7d). In all cases, the effective-medium predictions of surface modes have been calculated by the use of Eq. (33), as depicted by the solid line in Fig. 7b,c,d. The excellent agreement between the results of the continuum and structured materials can be verified.

In what follows, we demonstrate the non-reciprocal Rayleigh waves by full-wave numerical simulations of the elastic matrix with the gyroscopic inclusion. The wave responses by gyroscopic composites and their effectively homogeneous materials under a time-harmonic displacement applied on the central point of the top surface at the frequency 2 kHz are shown in Fig. 8. When $\alpha_1 = 0$, surface waves excited near the edge can be seen and their wave responses are exactly symmetric in two opposite directions. Asymmetric Rayleigh waves are caused when the spinner constant $\alpha_1 = \rho_1$ is introduced.

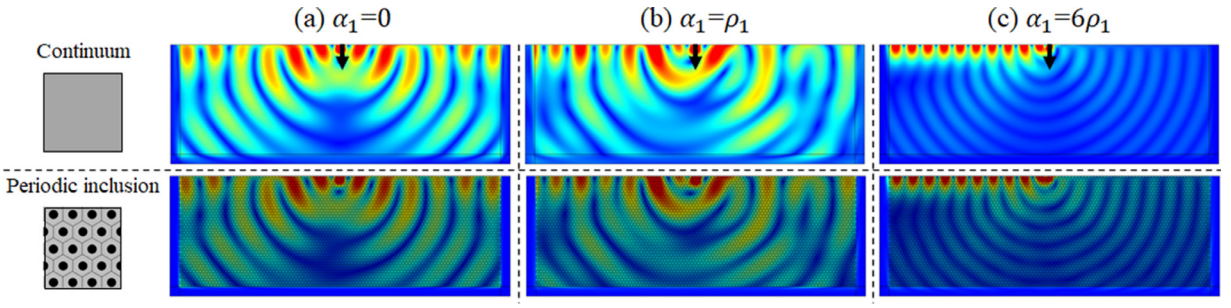

Fig. 8. The displacement responses of gyroscopic composites with periodic inclusions and their effectively homogeneous materials under a time-harmonic displacement (whose direction is represented by the arrow) applied on the central point of the top surface at the frequency 2 kHz in three cases: (a) α_1=0, (b) α_1=ρ_1, and (c) α_1= 6ρ_1.

Particularly for the case of $\alpha_1 = 6\rho_1$, the unidirectional waveforms are indeed created and in agreement with the prediction by Fig. 7d. In three cases, the displacement response for continuum medium and periodic composites coincides very well.

5. Conclusion

The gyro lattice with the mechanical quantum Hall effect has been demonstrated to possess the topologically protected unidirectional edge state as a result of the breaking of time-reversal symmetry. In the homogenization limit, this type of lattices can be equivalently regarded as a gyroscopic continuum medium that follows a new set of elastodynamic equations with the Hermite mass density tensor. The motivation of our study is to provide an understanding of this unusual edge state by setting up surface state equations for gyroscopic continua.

In this paper, a generic theory based on the Stroh formalism was established to analyze the surface states of the gyroscopic medium in the most general case of anisotropic elasticity. By considering the chiral density, the Stroh formulation was significantly modified to yield new forms of eigenvalue equations for solving surface wave speeds. The explicit analytic formulations of the theory are illustrated in the isotropic elasticity scheme. Dissimilar wave speeds in two opposite directions are predicted, showing the excellent agreement with direct numerical simulations of the non-reciprocal wave responses of gyroscopic elastic medium. In the reduced case, the developed theory predicts the reciprocal Rayleigh waves when the off-diagonal gyro coupling term of the Hermite density, which is the core factor of breaking the time-reversal symmetry, vanishes. The initially elliptical polarization mode of the particle motion at shallow depths tends to be converted into the transverse mode as the magnitude of this coupling term increases.

To realize the microstructure design of gyroscopic solids with the chiral inertial coupling, a generic homogenization method that relies on the surface response to external excitation is proposed for estimating effective material parameters of gyroscopic composite materials. The homogenization method could be used to retrieve all effective parameters of the gyroscopic materials from modal fields of either quasi-longitudinal or quasi-transverse dispersion branch, in distinct contrast to the previous method that can only treat the non-gyro composite with the presence of both L and T modes. In numerical examples, effective stiffness and chiral densities are retrieved for the composite material consisting of gyroscopic cylinders embedded in an elastic matrix. The non-reciprocal wave responses of gyroscopic composites with periodic inclusions and their effectively homogeneous materials are in good agreement for various spinner constants of gyroscopic cylinders.

Declaration of competing interest

The authors declare that they have no known competing financial interests or personal relationships that could have appeared to influence the work reported in this paper.

CRediT authorship contribution statement

Yuchen Zhao: Methodology, Software, Investigation, Validation. **Xiaoming Zhou:** Conceptualization, Supervision, Methodology, Writing - original draft, Visualization. **Guoliang Huang:** Investigation, Writing - review & editing, Visualization.

Acknowledgement

This work was supported by the National Natural Science Foundation of China (grant numbers 11872111, 11991030, 11991033, 11622215, 11521062, and 11572039) and 111 project (grant number B16003). G.H. acknowledge the support by the Air Force Office of Scientific Research under Grant No. AF 9550–18–1–0342 with Program Manager Dr. Byung-Lip (Les) Lee.

References

Assouar, M.B., Oudich, M., 2011. Dispersion curves of surface acoustic waves in a two-dimensional phononic crystal. Appl. Phys. Lett. 99, 123505.
Brun, M., Jones, I.S., Movchan, A.B., 2012. Vortex-type elastic structured media and dynamic shielding. P. Roy. Soc. A-Math. Phy. 468, 3027–3046.
Carta, G., Brun, M., Movchan, A.B., Movchan, N.V., Jones, I.S., 2014. Dispersion properties of vortex-type monatomic lattices. Int. J. Solids Struct. 51, 2213–2225.
Chadwick, P., Smith, G.D., 1977. Foundations of the theory of surface waves in anisotropic elastic materials. Adv. Appl. Mech. 17, 303–376.
Chen, H., Yao, L.Y., Nassar, H., Huang, G.L., 2019. Mechanical quantum Hall effect in time-modulated elastic materials. Phys. Rev. Appl. 11, 044029.
Cheng, Y., Zhou, X., Hu, G., 2017. Broadband dual-anisotropic solid metamaterials. Sci. Rep. 7, 13197.
Colquitt, D.J., Colombi, A., Craster, R.V., Roux, P., Guenneau, S.R.L., 2017. Seismic metasurfaces: sub-wavelength resonators and Rayleigh wave interaction. J. Mech. Phys. Solids 99, 379–393.
Ding, Y., Peng, Y., Zhu, Y., Fan, X., Yang, J., Liang, B., Zhu, X., Wan, X., Cheng, J., 2019. Experimental demonstration of acoustic Chern insulators. Phys. Rev. Lett. 122, 014302.
Fleury, R., Sounas, D.L., Sieck, C.F., Haberman, M.R., Alù, A., 2014. Sound isolation and giant linear nonreciprocity in a compact acoustic circulator. Science 343, 516–519.
Fu, Y.B., 2007. Hamiltonian interpretation of the Stroh formalism in anisotropic elasticity. P. Roy. Soc. A-Math. Phy. 463, 3073–3087.
Fu, Y.B., Rogerson, G.A., Wang, W.F., 2013. Surface waves guided by topography in an anisotropic elastic half-space. P. Roy. Soc. A-Math. Phy. 469, 20120371.
Haldane, F.D.M., 1988. Model for a quantum Hall effect without Landau levels: condensed-matter realization of the "parity anomaly". Phys. Rev. Lett. 61, 2015–2018.
Hasan, M.Z., Kane, C.L., 2010. Colloquium: topological insulators. Rev. Mod. Phys 82, 3045–3067.
Li, G.-.Y., Xu, G., Zheng, Y., Cao, Y., 2018. Non-leaky modes and bandgaps of surface acoustic waves in wrinkled stiff-film/compliant-substrate bilayers. J. Mech. Phys. Solids 112, 239–252.
Liu, X.N., Hu, G.K., Huang, G.L., Sun, C.T., 2011. An elastic metamaterial with simultaneously negative mass density and bulk modulus. Appl. Phys. Lett. 98, 251907.
Milton, G.W., Willis, J.R., 2007. On modifications of Newton's second law and linear continuum elastodynamics. P. Roy. Soc. A-Math. Phy. 463, 855–880.
Mori, T., Tanaka, K., 1973. Average stress in matrix and average elastic energy of materials with misfitting inclusions. Acta Metall 21, 571–574.
Nash, L.M., Kleckner, D., Read, A., Vitelli, V., Turner, A.M., Irvine, W.T.M., 2015. Topological mechanics of gyroscopic metamaterials. P. Natl. Acad. Sci. USA 112, 14495–14500.
Parker, D.F., 2013. The Stroh formalism for elastic surface waves of general profile. P. Roy. Soc. A-Math. Phy. 469, 20130301.
Rayleigh, L., 1885. On waves propagated along the plane surface of an elastic solid. P. Lond. Math. Soc. 1, 4–11.
Stroh, A.N., 1962. Steady state problems in anisotropic Elasticity. J. Math. Phys. Camb. 41, 77–103.
Tanuma, K., 2007. Stroh formalism and Rayleigh waves. J. Elasticity 89, 5–154.
Wang, P., Lu, L., Bertoldi, K., 2015. Topological phononic crystals with one-way elastic edge waves. Phys. Rev. Lett. 115, 104302.
Wu, T.-.T., Huang, Z.-.G., Lin, S., 2004. Surface and bulk acoustic waves in two-dimensional phononic crystal consisting of materials with general anisotropy. Phys. Rev. B. 69, 094301.
Zhou, X., Assouar, M.B., Oudich, M., 2014. Acoustic superfocusing by solid phononic crystals. Appl. Phys. Lett. 105, 233506.
Zhou, X., Zhao, Y., 2019. Unusual one-way edge state in acoustic gyroscopic continuum. Sci. China Phys. Mech. 62, 14612.